Journal of Environmental Chemical Engineering 9 (2021) 106575

Contents lists available at ScienceDirect

Journal of Environmental Chemical Engineering

journal homepage: www.elsevier.com/locate/jece

Phosphate removal from simulated wastewater using industrial calcium-containing solid waste

Donata Drapanauskaite [a,b], Kristina Buneviciene [a,b], Manoj Silva [a], Alvyra Slepetiene [b], Jonas Baltrusaitis [a,*]

[a] Department of Chemical and Biomolecular Engineering, Lehigh University, B336 Iacocca Hall, 111 Research Drive, Bethlehem, PA 18015, USA

[b] Lithuanian Research Centre for Agriculture and Forestry, Instituto al. 1, Akademija, Kedainiai district, LT-58344, Lithuania

A R T I C L E I N F O

Editor: Teik Thye Lim

Keywords:
Biomass ash
Lime kiln dust
Phosphate
Adsorption
Kinetics
Heavy metals

A B S T R A C T

Anthropogenic solid waste can serve as a reactive substrate to adsorb and immobilize PO_4^{3-} to enhance the sustainability of the water-energy-food nexus due to nutrient streams being recovered and recycled into the food chain as slow-release fertilizers. However, the structural complexity of solid waste presents significant hurdles identifying its ultimate potential to efficiently adsorb PO_4^{3-} from wastewater streams while its rich chemical composition – obtaining usable, heavy metal-free products to be reused in a highly regulated environment. In this study, two types of calcium-rich solid waste, biomass combustion bottoms ash (BA) and lime kiln dust (LKD), were evaluated for their propensity to adsorb PO_4^{3-} from simulated wastewater streams. Batch adsorption studies showed maximum adsorption (PO_4^{3-} removal) taking place at 2200 ppm of BA and 1800 ppm LKD with the sorption kinetics obeying well second order behavior. Estimated sorption capacity was 55.6 and 35.3 mg P/g LKD and BA, respectively, comparable or higher than for other natural Ca-containing natural minerals reported in the literature. PO_4^{3-} ion adsorption was shown to be inhibited to below 50% as organic acid concentration increased in simulated wastewater solution. Importantly, heavy metal release into the simulated wastewater was assessed and it was concluded that only BA released Zn concentrations which were higher than those regulated by EPA. Mechanistically, the underlying metal release phenomena were observed and explained by the significant initial material dissolution rather than by any competing processes, such as organic acid competitive adsorption with PO_4^{3-} ion.

1. Introduction

The world is experiencing unprecedented economic growth and an increase in the human population, thereby requiring more sustainable utilization of natural resources [1]. Plant nutrient recovery from anthropogenic waste streams, such as municipal or agricultural wastewater [2–4], is of major importance since these streams contain considerable amounts of nitrogen (N) and phosphorus (P) in the form of aqueous ammonium (~500 to ~1000 mg/L NH_4^+) [5,6] or phosphate (~600 to ~1000 mg/L PO_4^{3-}) [5,7] ions, with concentration depending on the source and pH of the wastewater [5,8]. If untreated, this wastewater can enter the watershed causing undesirable environmental effects including eutrophication [7,9,10]. Phosphorus scarcity and its sustainable use have been of particular interest since P is a key building block of living organisms that can‘t be manufactured or destroyed [11]. The most utilized technique to recover P in the form of PO_4^{3-} is its precipitation/crystallization as magnesium or calcium salts [5,12,13]. The resulting solid, low solubility and slow nutrient release PO_4^{3-} materials are typically struvite ($MgNH_4PO_4.6H_2O$) while the calcium PO_4^{3-} analog ($CaNH_4PO_4.7H_2O$) is very unstable and decomposes at room temperature to hydroxyapatite ($Ca_5(PO_4)_3OH$) [14]. Other calcium PO_4^{3-}-containing crystalline materials, such as brushite ($CaHPO_4{\cdot}2H_2O$), or even amorphous calcium phosphate^{-} have been observed under different reaction conditions such as pH, temperature, supersaturation level and Ca/P molar ratio [12]. Calcium chloride has chiefly been used as a calcium source due to its high water solubility [12,15–17]. Cumulative energy demand associated with calcium chloride produced via the Solvay process and made from brine is 11.8 MJ kg^{-1}, much greater than that for low solubility calcium source, calcium carbonate, which is mined in a powder form with 0.68 MJ kg^{-1} [18]. As municipal wastewater treatment plants (WWTPs) begin shifting to the new paradigm of water resource recovery rather than waste production [19],

* Corresponding author.
E-mail address: job314@lehigh.edu (J. Baltrusaitis).

https://doi.org/10.1016/j.jece.2021.106575
Received 31 May 2021; Received in revised form 3 September 2021; Accepted 10 October 2021
Available online 13 October 2021

sustainability and availability of low environmental footprint calcium sources become an issue and low solubility calcium-containing materials are currently evaluated to assess their potential for PO_4^{3-} recovery from wastewater. Natural Ca-rich clays, such as sepiolite [20], calcite-coated phyllosilicates [21] or other calcium-rich natural minerals [22] have been utilized for PO_4^{3-} recovery as well as other abundantly available processed materials or waste [23–25]. Very recent developments, however, have been considering the suitability of calcium-rich industrial waste [26]. In particular, every year a large amount of calcium-containing biomass combustion ash is generated (Denmark 31 kton, Austria 133 kton, The Netherlands 234 kton, Italy 250 kton, Sweden 528 kton, Canada >1000 kton) [27] as the use of biomass for electricity generation as well as for heating and cooling has become more prevalent [28]. Depending on the source of biomass ash (BA), it contains a complex and heterogeneous mixture of inorganic crystalline and amorphous minerals [29,30]. Biomass ash is typically enriched in calcium (Ca) with other nutrients, such as potassium (K), magnesium (Mg) as well as some phosphorus (P) and sulfur (S) [31,32]. Also, elements considered as micronutrients, such as iron (Fe), manganese (Mn) and titanium (Ti) are present [33] with small amounts of other heavy metals. The amounts of ash generated are not insignificant and in developing countries can account for up to 60% of the total municipal solid waste [34]. Few reports exist on BA interactions with PO_4^{3-} [35,36] but already showed the potential. Up to 97% PO_4^{3-} recovery was observed with BA 9.05 g/L via surface facilitated adsorption [35]. Solution pH dependence was observed when 10 ppm PO_4^{3-} was adsorbed on BA with low pH values resulting in the highest removal efficiency [36]. Alternatively, lime kiln dust (LKD), a byproduct collected by dust control systems from burning limestone, contains high calcium concentrations and is currently chiefly used as a soil stabilizer. Together, these two constitute high calcium concentration industrial waste that has a direct potential to recover PO_4^{3-} from wastewater streams without the need for soluble or mined natural calcium sources.

The purpose of this study is to assess the performance of these two calcium-rich industrial waste sources, BA and LKD, for their PO_4^{3-} removal ability and the resulting release of any heavy metals due to the interaction with organic molecules routinely present in anthropogenic wastewater. PO_4^{3-} sorption isotherms and the resulting kinetics information were obtained using batch experiments. Moreover, trace metal presence was also quantified as industrial solid waste contains metals that may act as micronutrients [31] or exhibit biotoxicity above critical concentrations. Of particular interest was PO_4^{3-} removal in the presence of low molecular weight dicarboxylic acids. Gluconic, glyceric, glucuronic, glucaric and tartaric acids are generally known as sugar acids and are oxidation products of sugars [37] hence abundantly present in wastewater since the dissolved organic compounds mainly consist of ethanol, tartaric acid/tartrates, microbial biomass (mainly yeasts) and phenolics [38,39]. For example, tartaric acid was previously found to reduce Cr(VI) to Cr(III) in the soil, chiefly in the liquid environment, and to affect the mobility of heavy metals due to their desorption, complexation, and precipitation [40]. Hence, the leaching of the heavy metals during PO_4^{3-} recovery in the presence of several dicarboxylic acids was investigated and quantified.

2. Materials and methods

2.1. Reagents

BA and LKD were obtained from manufacturers in Lithuania. LKD used in this study was obtained from *JSC Naujasis Kalcitas*, Naujoji Akmene, Lithuania and BA obtained from *JSC Mortar Akmene* by burning wood pellets. All reagents for chemical analysis were obtained reagent grade from Fischer Scientific and used as received. Double distilled water was used in all experiments.

2.2. Adsorption experiments

Due to the complexity of solid waste materials, model wastewater was utilized. Simulated NH_4^+ and PO_4^{3-} containing wastewater samples were prepared by adding 600 ppm of monoammonium phosphate, MAP ($NH_4H_2PO_4$, 99.9%, Fisher Scientific) in 18.2 MΩ/cm deionized water (Millipore, USA). A 600 ppm MAP solution represents PO_4^{3-} and NH_4^+ values found in municipal, animal and industrial wastewater [41]. The optimal amount of the BA or LKD was determined by increasing the concentration from 200 to 2200 ppm range until PO_4^{3-} adsorption achieved a steady state. 600 MAP solution was prepared with and without organic acid dissolved by dissolving solid salts or organic acids in deionized water and solid adsorbent was added while stirring. Aliquots of 1 mL were sampled periodically, filtered through a 0.22 µm polyethersulfone filter, and analyzed using ion chromatography.

2.3. Characterization of sorbents

The X-ray powder diffraction (XRD) data were obtained with a DRON-6 X-ray diffractometer with Bragg–Brentano geometry using Ni-filtered CuK_α radiation, operating at a voltage of 30 kV and an emission current of 20 mA. The step-scan spanned the angular range from 10° to 60° (2θ) in steps of $2\theta = 0.02°$.

The surface morphology of materials was examined using the Thermo Fisher Scientific Phenom scanning electron microscope (SEM) at an accelerating voltage of 15 kV. SEM images were obtained using the secondary electron (SE) mode. The instrument was equipped with an energy dispersive spectrometer (EDS) system, for the analysis of the X-rays emitted by the samples to determine the elemental composition during SEM observations [42].

The BET surface areas of the samples were measured via nitrogen physisorption (−196 °C) using a Micromeritics ASAP 2020 instrument. Approximately 0.45 g of catalyst was used for each measurement. The specific surface area was calculated using the Brunauer-Emmett-Teller (BET) method. Before the measurement, the catalyst was evacuated at 60 °C until the degassing rate $< 10^{-4}$ mmHg/min was observed. In addition, Barrett-Joyner-Halenda (BJH) analysis was employed to determine pore size using adsorption and desorption isotherms. This technique characterizes pore size distribution independent of the external area due to the particle size of the sample.

A chemical analysis of the materials, used in the experimental investigation, was carried out. The samples were sieved, extracted with *aqua regia* and then analyzed with Perkin Elmer Optima 2100 DV ICP–OES spectrometer (Perkin Elmer, USA). Atomic Absorption Spectroscopy (AAS) (Perkin Elmer, USA) was used to find the concentration of Ca and Mg, flame photometer (FP) (Sherwood, UK) of K, UV–VIS spectrophotometer (Shimadzu, Germany) of P and inductively coupled plasma mass spectrometry (ICP–MS) (Thermo Fisher Scientific, USA) of heavy metals.

Total N was determined using the Kjeldahl method, total P_2O_5 using the spectrophotometric method with spectrophotometer Agilent Technologies Cary 60 UV-Vis (USA) in solid samples before and after the reaction (BA, LKD, 2200/600 ppm BA/MAP, 1800/600 ppm LKD/MAP, 2200/600/1000 ppm BA/MAP/TA and 1800/600/1000 ppm LKD/MAP/TA). Determination of C_{org} content according to oxidizability by spectrophotometric method with spectrophotometer Agilent Technologies Cary 50 UV-Vis (USA) in the same samples. Water-soluble P_2O_5 and total S (SO_4^{2-}) in solid and liquid samples (2200/600 ppm BA/MAP, 1800/600 ppm LKD/MAP, 2200/600/1000 ppm BA/MAP/TA and 1800/600/1000 ppm LKD/MAP/TA), total N and total P_2O_5 in liquid samples was determined using the spectrophotometric method (spectrophotometer HACH LANGE DR3900, Germany). Total: K_2O, Ca, Mg and water-soluble: K_2O, Ca, Mg was determined using the atomic absorption spectrometry method (atomic absorption spectrometer PerkinElmer precisely AAnalyst 200, USA).

Raman spectra and spectral maps were acquired using WITec alpha300R confocal Raman microscope using 532 nm laser, Zeiss EC Epiplan-Neofluar x100 / 0.9 objective, G2: 600 g/mm grating, 3 s integration time per point for *ex situ* study. For in situ studies, 532 nm laser, Zeiss x20 / 0.4 objective, and G2:600 g/mm grating were used. In both studies, the spectral range was 100–4000 cm^{-1} with the center at 2000 cm^{-1} and the spectral resolution was ~2 cm^{-1}. Before each experiment, the instrument was calibrated using a Si wafer. The laser intensity at the sample was ~54 mW. Spectral maps were typically acquired using 2–4 s exposure time per single scan point. To elucidate heterogeneity of a single particle, 2-D spectral maps were acquired in the x-z plane, e.g. parallel to the direction of the beam.

The True Component Analysis (TCA) was used to create spectral intensity distribution images of different spectra components. It is utilizing a linear combination of the spectral components using the basis analysis algorithm via Eq. (1).

$$\overrightarrow{S_i} = \widehat{B}\,\overrightarrow{H_i} + \overrightarrow{E_i} \quad (1)$$

where $\overrightarrow{S_i}$ – spectrum i from the spectral dataset, $\widehat{B}$ – matrix of basis spectra, $\overrightarrow{H_i}$ – mixing values of spectrum i, $\overrightarrow{E_i}$ – error spectrum. The mixing values are fitted using least-squares minimization methods following the expression (2).

$$\left(\overrightarrow{S_i} - \widehat{B}\,\overrightarrow{H_i}\right)^2 = \text{minimum} \quad (2)$$

3. Results and discussion

3.1. Batch PO_4^{3-} adsorption experiments

PO_4^{3-} adsorption screening study was initially carried out with 600 ppm MAP solution and different initial concentrations of the adsorbent at a constant temperature of 18 °C. Twelve experiments of initial BA and LKD (200, 300, 500, 600, 800, 1000, 1200, 1500, 1600, 1800, 2000, 2200 and 2500 ppm) concentrations were used. The flasks were stirred for 24 h to ensure the reaction equilibrium. It can be seen in Fig. 1 that the amount of PO_4^{3-} removed increased with the increasing initial adsorbent concentration ranging from 200 to 2500 ppm. The initial tendency to remove PO_4^{3-}, however, decreased slightly after 1000 ppm LKD and 1600 ppm BA indicating potentially two different PO_4^{3-} removal mechanisms present. Overall, ~95% PO_4^{3-} removal was achieved with 1800/600 ppm LKD/MAP while ~78% of PO_4^{3-} was removed with 2200/600 ppm BA/MAP. These two solid adsorbent concentrations were selected as optimal for all kinetic experiments.

3.2. Chemical and crystalline characterization of as-received BA and LKD and after PO_4^{3-} adsorption

The full chemical composition of BA and LKD is shown in Table 1

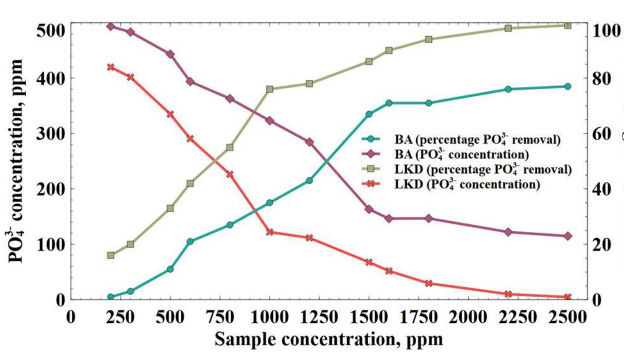

Fig. 1. Measured PO_4^{3-} concentration in residual solution and percentage of PO_4^{3-} removed using increasing initial concentrations of LKD and BA. The initial concentration of MAP was 600 ppm and the initial solution pH was 5.4.

Table 1
Chemical composition of as received a solid BA and LKD powders.

Parameter	BA solid	LKD solid
Total P, mg/kg	17,195 ± 134	530 ± 0
Citrate-soluble P, mg/kg	1,206 ± 189	26.42 ± 4
Water-soluble P, mg/kg	58.1 ± 3.7	57.2 ± 1.23
Total K, mg/kg	54,105 ± 969	1,625 ± 7
Water-soluble K, mg/kg	7,580 ± 28	520 ± 0
Total Ca, mg/kg	440,030 ± 7,043	568,605 ± 1,223
Citrate-soluble Ca, mg/kg	75,531 ± 5,663	136,405 ± 17,593
Water-soluble Ca, mg/kg	59,538 ± 124	10,9313 ± 18,615
Total Mg, mg/kg	29,905 ± 841	12,765 ± 431
Citrate-soluble Mg, mg/kg	1,269 ± 315	705.5 ± 37
Total S, mg/kg	5,867 ± 1280	9,967 ± 1,452
Citrate-soluble S, mg/kg	5,623 ± 114	5,388 ± 762
Water-soluble S, mg/kg	5,536 ± 101	5,113 ± 781

with a graphical representation of major nutrients (P, K, Ca, Mg and S) as well as residual Al and Fe shown in Fig. 2a.

Both are comprised chiefly of Ca^{2+} containing chemical compounds with Ca accounting for ~50–92% of major nutrients measured in this study by weight according to Fig. 2a. Other plant nutrients, such as Mg, K and P, comprise the remainder. LKD, in particular, contains high calcium amounts depending on whether high-calcium lime or dolomitic lime is processed [43]. According tot he literature, typical composition of LKD varies from 31% to 55% CaO with significantly smaller concentrations of other elements (1.7–9.9% SiO_2, 0.7–4.1% Al_2O_3, 0.03–0.22% K_2O, 0.5–25% MgO) [44–46]. Notable was residual phosphorus content in BA of ~5% by weight of all major nutrients since P is a primary nutrient necessary to the plants. Al and Fe were present in both BA and LKD. It needs to be stressed that soluble Al^{3+} form at low pH is toxic to the plants directly or by binding phosphorus into insoluble compounds [47]. However, this effect only becomes apparent when soil pH reaches below 5.5, e.g. in relatively acidic soil [48,49]. Fe is a nutrient that is required for normal plant growth and reproduction [47]. However, soil that is alkaline or has a significant amount of lime added often causes an iron deficiency in the plants as it becomes unavailable for plant adsorption [50].

P increase in 2200/600 ppm BA/MAP and 1800/600 ppm LKD/MAP solid materials was particularly noticeable in Fig. 2b as it increased by ~x3 and fold, respectively. These early findings suggested that BA and LKD can be viable PO_4^{3-} adsorption materials and yield sizeable concentrations of this nutrient in the solid phase. The adsorption process in an aqueous solution, however, dramatically modified the physical particle properties of both BA and LKD as shown in Fig. 2c and d, respectively. Before the reaction, as-received materials were particular with the measured particle size of 10–20 µm. After the reaction, distinct particle size decreased as materials underwent partial dissolution resulting in flake morphology of the smaller particle agglomerates. Spatially resolved SEM in combination with EDS was further utilized to investigate the distribution of elements within these reacted particles and allowed observing the dispersion of the major elements and their incorporation into the calcium oxide and calcium carbonate minerals. It can be seen in Fig. 3 that in both reacted cases of 2200/600 ppm BA/MAP and 1800/600 ppm LKD/MAP elements detected under EDS were chiefly dispersed at the micron level with P uniformly distributed across the particle agglomerates mapped. This suggests that reacted materials uniformly adsorb PO_4^{3-} and can potentially serve for its controlled release.

Table 2 summarizes EDS measured weight concentrations of major elements and their corresponding oxides in the solid material after the reaction of 600 ppm MAP with 2200/600 ppm BA/MAP and 1800/600 ppm LKD/MAP. In particular, P_2O_5 concentrations of up to 36% were detected for 2200/600 ppm BA/MAP, quite comparable to those currently utilized in mineral phosphorus fertilizers. Notable is the difference in concentrations as measured using bulk techniques in Fig. 2b with EDS which largely measures surface information from a few micro

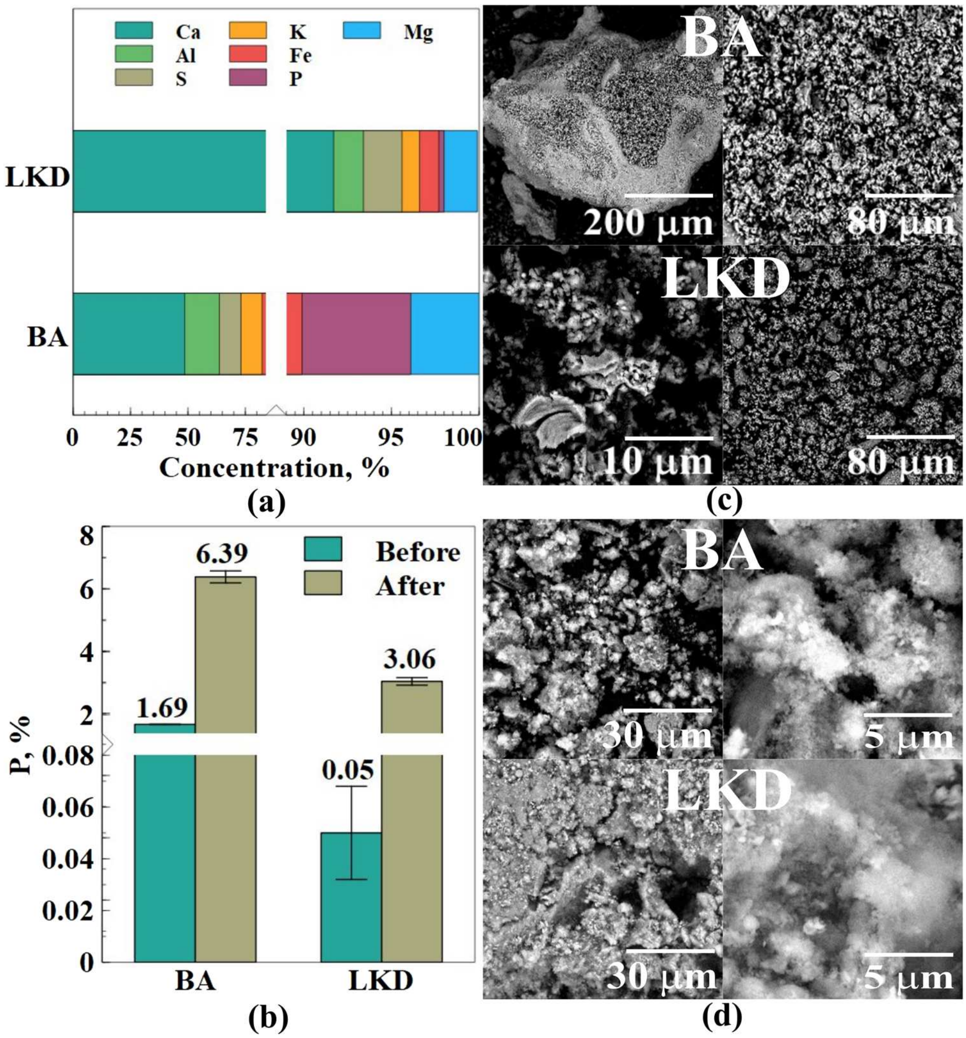

Fig. 2. (a) Chemical composition of the major nutrient elements in BA and LKD. (b) Measured bulk phosphorus concentration before and after the reaction of 2200/600 ppm BA/MAP and 1800/600 ppm LKD/MAP. (c) SEM images of as-received BA and LKD. (d) SEM images of reacted BA and LKD.

electron beam/sample interaction volumes. This can be rationalized by the mass transfer limitation of the process whereby PO_4^{3-} is chiefly concentrated on the particle surface with the diffusion being limited.

X-ray diffraction (XRD) measurements were used to elucidate the crystallinity of BA and LKD powders. The results are shown in Fig. 4a and b. This mineralogical characterization using XRD patterns showed distinct crystalline phases. The obtained data confirmed the presence of several major crystalline phases in the as-received materials. The main crystalline phase in BA was CaO [51–53] with the main peaks at 2θ of 32 and 37° and $CaSiO_3$ [54] and quartz in a complex mixture. The predominant crystalline phase in LKD was calcite – $CaCO_3$ [55] - with the main peak at 2Θ of 29°, accompanied by smaller quantities of quartz – SiO_2 [56] and calcium hydroxide $Ca(OH)_2$ [57]. The XRD analysis of reacted materials showed two different behaviors. BA crystalline structure was significantly perturbed with the peaks almost disappearing or significantly changing suggesting strong dissolution or amorphization of the particles, consistent with the SEM data in Fig. 2d. LKD, on the other hand, exhibited only minor crystalline changes upon PO_4^{3-} adsorption and largely retained its crystalline order. Interestingly, XRD did not provide conclusive evidence in the formation of any crystalline phosphates implying amorphous internalized or adsorbed PO_4^{3-} nature. This interesting behavior was further elucidated using BET analysis where, after the adsorption experiments, there was a significant increase in the measured BET surface area. In particular, it increased from 2 and 5 m^2/g to 35 and 29 m^2/g for BA and 2200/600 ppm BA/MAP and LKD and 1800/600 ppm LKD/MAP, respectively. While as received BA was a non-porous material as it can be seen in Fig. 4d, it developed a significant amount of porosity with a pore size of up to 1000 Å, similar behavior to that observed for LKD.

The amorphous nature of the material formed warranted a detailed analysis using Raman spectroscopy which can provide detailed information on the structure of the adsorbed PO_4^{3-} ion [58,59].

Raman peak assignments of the post PO_4^{3-} adsorption will be based on the existing fundamental data [60,61] based on changes in ion symmetry through the series PO_4^{3-} (T_d symmetry), HPO_4^{2-} (pseudo - C_{3v}), $H_2PO_4^{-}$ (C_{2v}, or lower), H_3PO_4 (lower than pseudo-C_{3v}). In particular, while Raman spectra of as received LKD showed a strong peak at 1080 cm^{-1} due to the ν_1 (CO_3^{2-}) of $CaCO_3$, as received BA did not exhibit any peaks in Raman spectra (not shown). After 2200/600 ppm BA/MAP and 1800/600 ppm LKD/MAP reaction, however, new peaks were observed in both cases. Representative spectral components derived from TCA and their corresponding spectral maps are shown in Fig. 5 for (a) 2200/600 ppm BA/MAP and (b) 1800/600 ppm LKD/MAP. The most relevant was phosphate peak likely originating from hydroxyapatite, $Ca_5(PO_4)_3(OH)$, which can be characterized by the characteristic vibration band of PO_4^{3-} groups 960–962 cm^{-1}, while amorphous calcium PO_4^{3-} exhibits a most characteristic shift by a 10 cm^{-1} towards ~950 cm^{-1} [62]. Another peak at 1020–1080 cm^{-1} observed typically overlaps with that of ν_1 (CO_3^{2-}) of $CaCO_3$ [63,64]. The peaks at 848–853 cm^{-1} are more difficult to assign since they can

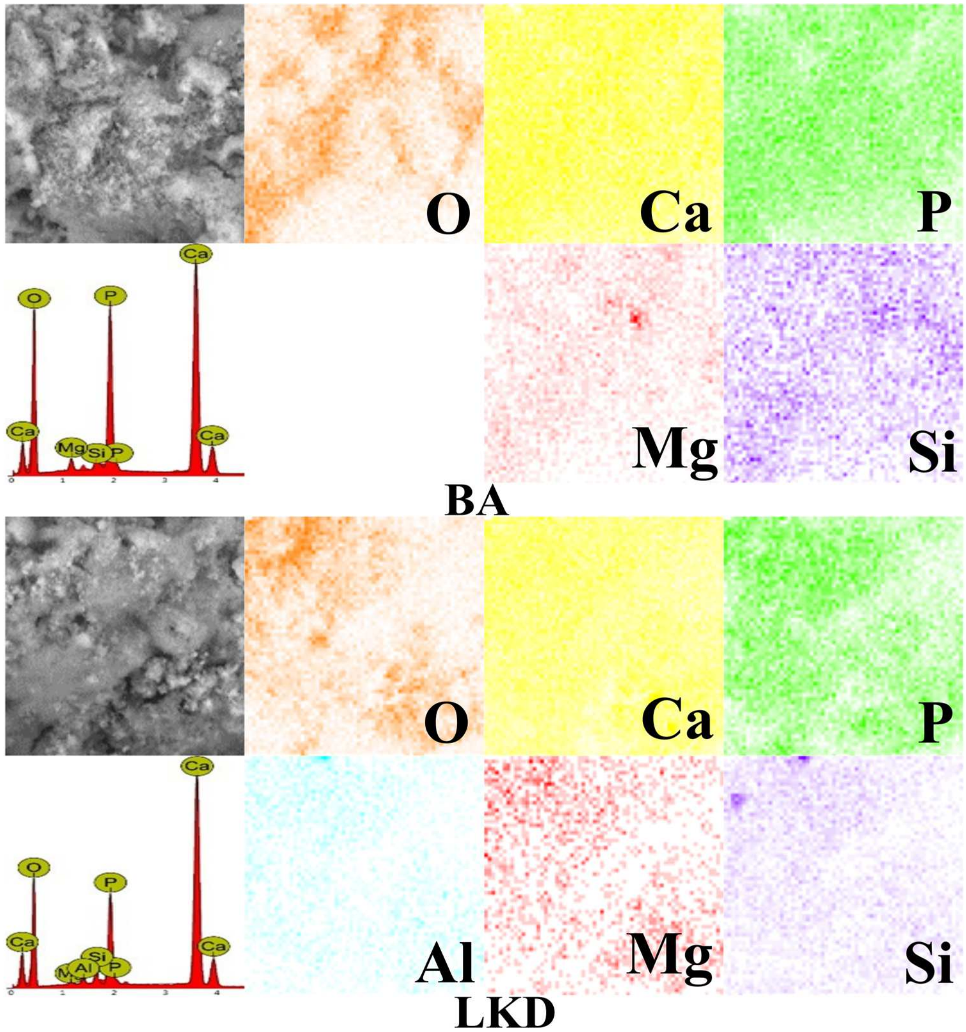

Fig. 3. Secondary electron images were obtained using SEM (in gray) and the corresponding EDS elemental maps (shown in colors) of 2200/600 ppm BA/MAP and 1800/600 ppm LKD/MAP.

Table 2
EDS determined concentrations in weight % of major elements and their corresponding oxides.

Element	Weight Concentration (%) BA	Oxide	Oxide Weight Concentration (%)	Weight Concentration (%) LKD	Oxide	Oxide Weight Concentration (%)
O	50.8	–	–	47.59	–	–
Ca	33.4	CaO	57.9	41.1	CaO	69.5
P	12.8	P_2O_5	36.3	8.9	P_2O_5	24.7
Mg	1.0	MgO	2.1	0.6	MgO	0.9
Si	0.8	SiO_2	2.2	1.3	SiO_2	3.3
Al	–	–	–	0.7	Al_2O_3	1.5

likely be associated with P-OH or P-$(OH)_2$ stretches although they miss the corresponding complementary vibrations originating from the PO_4^{3-} ion symmetry split upon adsorption [65]. Further, since they comprise rather a large portion of the reacted BA material surface as shown in Fig. 5a, they likely can be related to more complex calcium silicates rather than PO_4^{3-} ion vibration [66]. Other peaks below 750 cm^{-1} were non-specific or of low intensity supporting the amorphous nature of adsorbed PO_4^{3-} ion and integral CO_3^{2-} remaining originating from $CaCO_3$ in LKD as shown in Fig. 5b.

3.3. PO_4^{3-} sorption isotherms and kinetic study

Tartaric acid (2,3-dihydroxysuccinic acid, further in the text referred to as TA) is a carboxylic acid that exists in various plants, such as grapes and tamarinds [67]. It represents a useful dicarboxylic acid molecule which in some wastewater streams has been found with concentrations of up to 1300 ppm [68] and has been shown, in general, to inhibit PO_4^{3-} sorption and crystallization of the solid products, such as struvite [5]. Fig. 6a shows the concentration profile (q, mg/g) of PO_4^{3-} ions adsorbed from 600 MAP solution by BA, LKD or LKD in the presence of 500 ppm TA.

It was observed that most of the PO_4^{3-} uptake by 1800 ppm LKD, 1800 ppm LKD in the presence of 500 ppm tartaric acid and 2200 ppm BA occurs within ~15 min. The equilibrium amount of PO_4^{3-} removed from solution was 63% on LKD, 53% on LKD in the presence of tartaric acid and 42% BA. After the initial 25 min, the uptake further increased

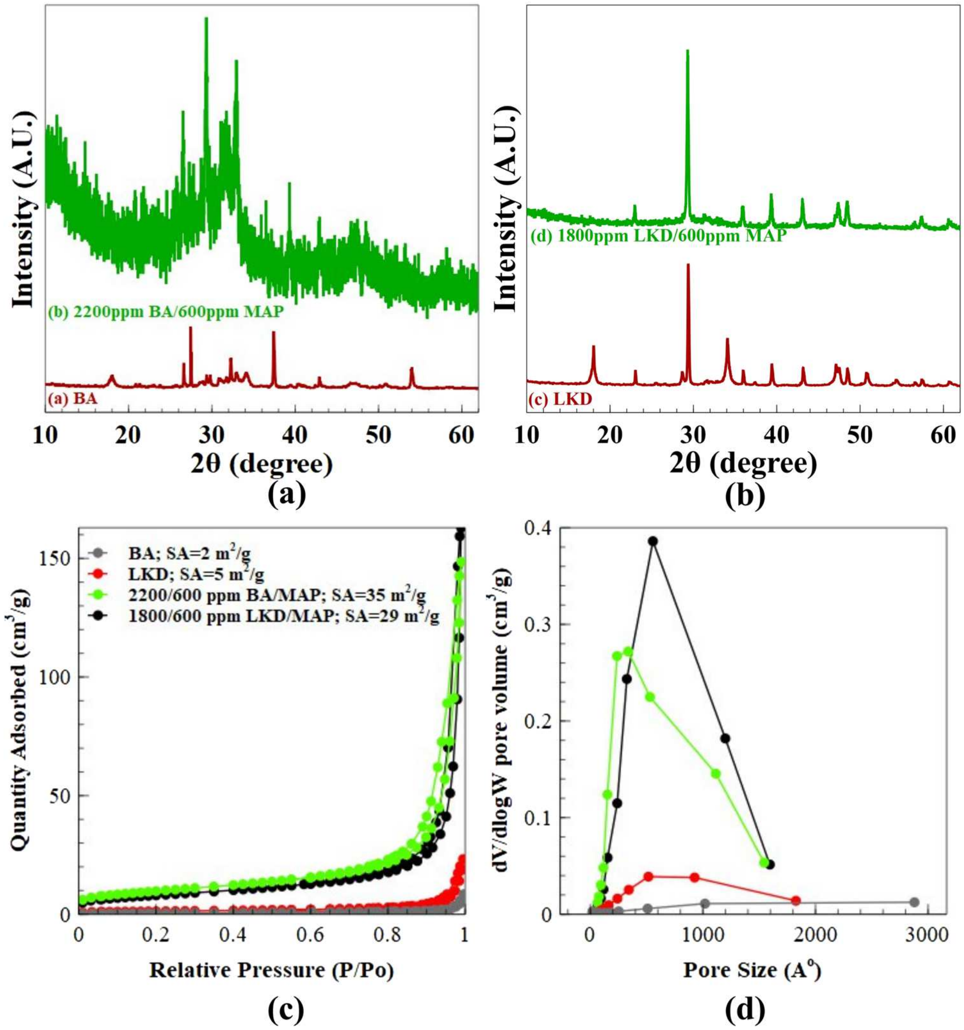

Fig. 4. XRD of (a) BA and 2200/600 ppm BA/MAP and (b) LKD and 1800/600 ppm LKD/MAP. Corresponding comparative (c) nitrogen physisorption and (d) BJH pore size distribution computed from the desorption branch for different minerals.

albeit at a much slower rate. The LKD exhibited the fastest initial rate of PO_4^{3-} removal with the PO_4^{3-} almost completely removed after 90 min. In the case of BA and LKD with tartaric acid, the rate of PO_4^{3-} removal was slower and achieved much lower equilibrium values.

The pH of the solution was measured to provide critical information on PO_4^{3-} adsorption and the following precipitation reactions and the data are shown in Fig. 6b. In particular, pH quickly rose to 8 and 9 for 2200 ppm BA and 1800 ppm LKD, respectively. At these pH values, hydroxyapatite has been shown to form [69]. Only for the highest concentration of OA did pH remain low around 3. Oxalic acid had the lowest pKa value among the organic acids tested. In this case, the highest pH value of 3 was achieved after 120 min with 2200 ppm BA while with 1800 ppm LKD it was 7.5 showing that BA had a much lower buffering capacity to provide alkaline ions needed to maintain elevated pH. This suggests that the presence of the organic acids will strongly influence the PO_4^{3-} ion removal by modulating solution pH, especially for BA and much less for LKD. However, only OA at the highest concentrations can inhibit phosphate adsorption due to the pH as the rest of the acids at 1000 ppm exhibited much higher pH values.

Further understanding of the sorption kinetics involved was pursued since it is necessary for the design of any large-scale adsorption facilities. Many models are used to fit PO_4^{3-} adsorption experiments to obtain quantitative kinetic parameters. Furthermore, to examine the mechanism of the adsorption processes, such as mass transfer and chemical reaction, a suitable kinetic model is needed to be applied to obtain the rate constants. In this work, two kinetic models [70–72] were used to model the adsorption kinetics of PO_4^{3-} onto BA and LKD. The kinetic equations including pseudo-second-order model [72], and Elovich model [71] used are described as follows

$$\text{Pseudo}-\text{second}-\text{order equation}: \frac{t}{q_t} = \frac{1}{k_2 q_e^2} + \frac{t}{q_e} \tag{3}$$

$$\text{Elovich equation}: q_t = \frac{ln a_e b_e}{b_e} + \frac{1}{b_e} lnt \tag{4}$$

where q_t is the adsorbed amount at time t, mg/g, q_e is the adsorbed amount at equilibrium, mg/g, k_2 is the rate constant of pseudo-second-order adsorption, g/(mg h); the parameter a_e is the initial adsorption rate, mg/(g h), and b_e is related to extent of surface coverage and activation energy for chemisorption, g/mg. The relative parameters (the derived rate constants together with the correlation coefficient R^2) of the pseudo-second-order and Elovich are in Table 3.

Constant k_2 was calculated from the intercept of the line by plotting t/q_t versus t in the pseudo-second-order model, while the initial adsorption rate a_e was calculated from the intercept of the line obtained by plotting q_t versus *lnt* in the Elovich equation. Figs. 7 and 8 show the corresponding plots in linearized form. Notably, pseudo-first order fits resulted in low R^2 values likely since pseudo-first order model is only valid in scenarios where the change in the bulk solution concentration of the adsorbate is small [70,73]. As such, the physical insight gained from

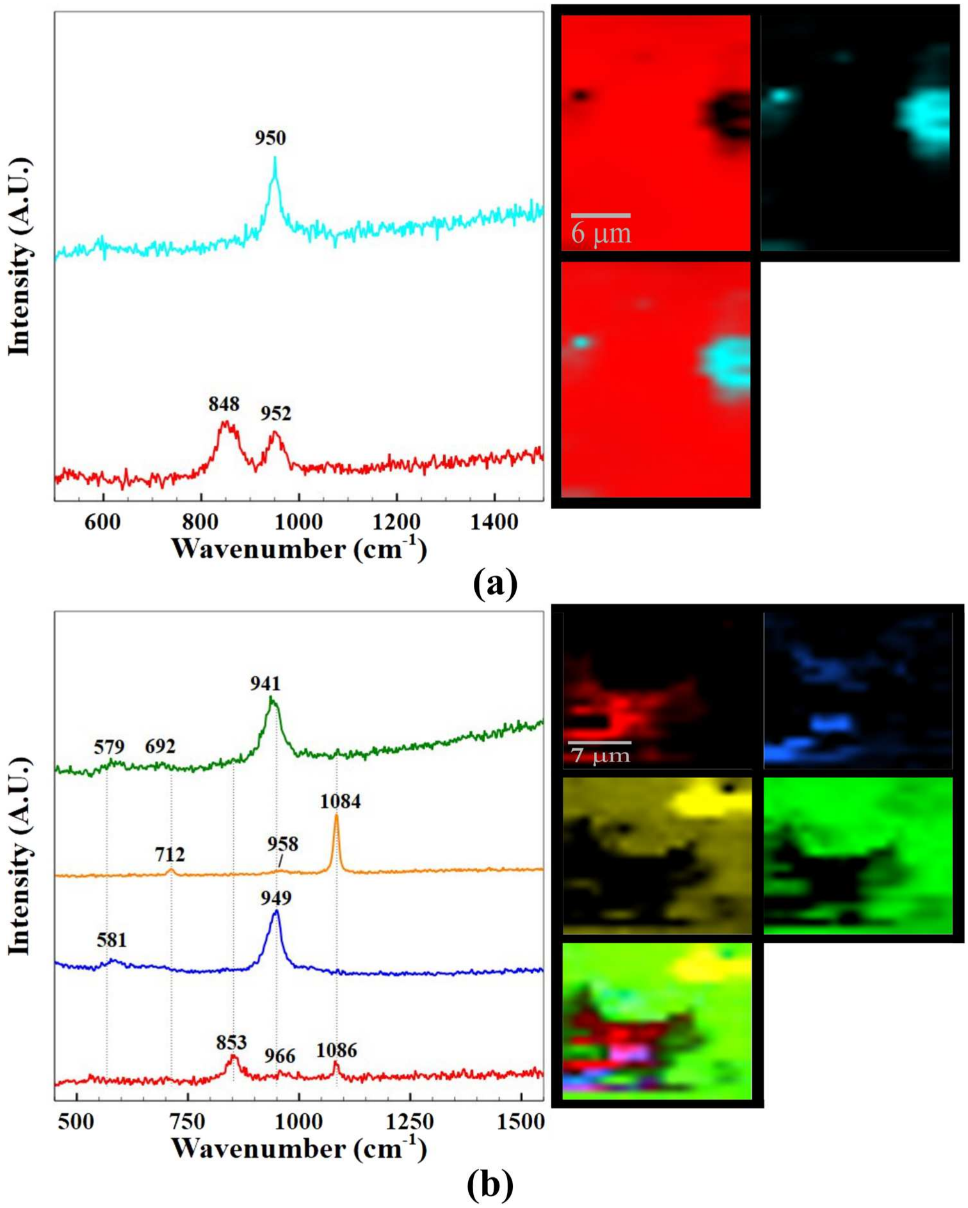

Fig. 5. Representative total components derived from Total Component Analysis and their corresponding spectral maps for (a) 2200/600 ppm BA/MAP and (b) 1800/600 ppm LKD/MAP.

the pseudo-second order fitting is that the adsorption is surface-reaction limited. Compared to previously reported natural minerals, such as Ca-rich sepiolite, which exhibits a q_e value of 32 mg P/g, and goethite which exhibited 34 mg P/g, both LKD and BA show higher phosphate adsorption capacities (Table 4) [20,74]. The higher q_e value is indicative of an adsorbent that can be utilized more efficiently given that a smaller mass of adsorbent can bind a higher concentration of PO_4^{3-}. The addition of tartaric acid leads to a reduction in the q_e for LKD, indicating that phosphate adsorption is hindered by the presence of the acid, due to surface dissolution of the adsorbent. In addition to the lower q_e value, a slightly lower pseudo-second-order rate constant is also observed for LKD in the presence of tartaric acid due to the suppressed PO_4^{3-} adsorption.

Comparing the correlation coefficients of two kinetic models, it is revealed that the pseudo-second-order model best fits the adsorption kinetic of PO_4^{3-} on LKD ($R^2 = 0.99$), LKD with tartaric acid ($R^2 = 0.99$), and BA ($R^2 = 0.97$).

Due to the marked difference observed in the equilibrium amount and the corresponding kinetics of PO_4^{3-} adsorption, sorption experiments were also performed utilizing other common organic acids present in the wastewater solutions from natural or anthropogenic sources. Those included, in addition to tartaric acid, citric, glycolic, oxalic and citric acids in the concentration range from 50 to 1000 ppm in the initially simulated wastewater also containing 600 ppm of MAP. The equilibrium removal results (e.g. maximum amount of PO_4^{3-} removed after the equilibrium was achieved) are tabulated in Table 5. Interesting dynamics were observed where citric and oxalic acids strongly inhibited the adsorption of PO_4^{3-} on 1800 ppm of LKD while glycolic acid did not result in strong inhibiting effects. Acid concentration dependence was also observed within the range of acids analyzed with 1000 ppm resulting in the greatest inhibition. Interestingly, oxalic acid exhibited a dramatic inhibition of PO_4^{3-} removal in the presence of 2200 ppm of BA. Two phenomena can be proposed to explain these data. First, solution pH, as suggested by Fig. 6**b**, remains at pH = 3 in the presence of the lowest pKa oxalic acid at 1000 ppm thus inhibiting precipitation. This effect is much less pronounced for LKD suggesting LKD possesses a much greater capacity to maintain the alkalinity of the solution pH. Second, organic acids strongly bind to the surface sites

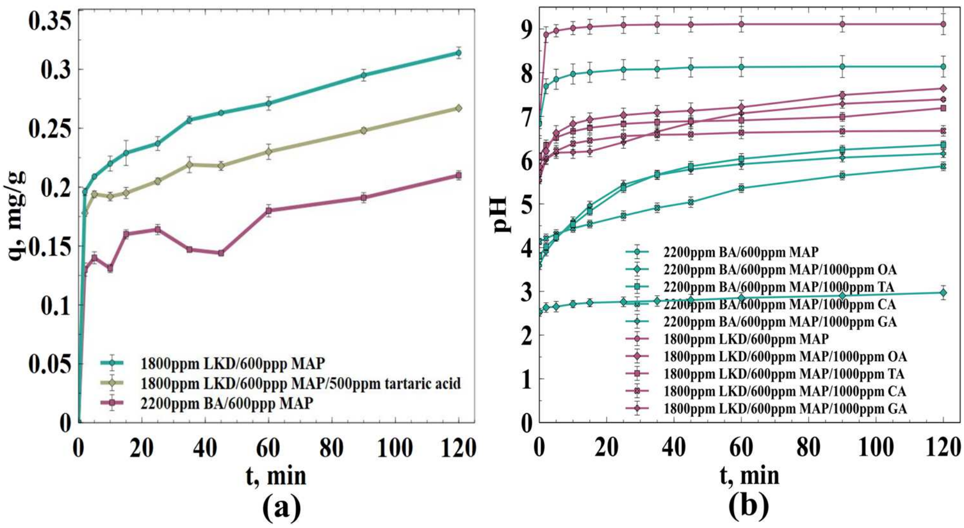

Fig. 6. (a) PO_4^{3-} removed by 1800 ppm LKD and 2200 ppm BA from 600 ppm MAP solution with no pH adjustment. (b) pH evolution with time of 1800 ppm LKD and 2200 ppm BA from 600 ppm MAP solution with and without 1000 ppm organic acids present. OA- oxalic acid, TA – tartaric acid, CA – citric acid and GA – glycolic acid.

Table 3
Calculated kinetic parameters for phosphorus sorption to BA, LKD and LKD in the presence of tartaric acid.

	Pseudo-second-order equation			Elovich Equation		
	q_e (mg P/g)	k_2 g (mg/h)	R^2	a_e	b_e	R^2
LKD	55.6	0.0013	0.99	4285	0.065	0.92
LKD+tartaric acid	46.8	0.0016	0.99	20,012	0.092	0.84
BA	35.3	0.0014	0.97	1930	0.11	0.69

responsible for PO_4^{3-} removal, likely calcium atoms – calcium is known to forming binding complexes with organic acids, such as oxalic [81], and thus inhibits the overall process. Furthermore, citric, tartaric, and oxalic acids can lead to the surface dissolution of the adsorbent, which would lead to lower PO_4^{3-} removal.

3.4. Spectroscopic characterization of the PO_4^{3-} adsorption products in the presence of organic acids

Raman characterization was performed of the 1800 ppm LKD surfaces reacted with 600 ppm MAP in the presence of tartaric, citric, glycolic and oxalic acids at low and high initial concentrations of acids (50, 500 and 1000 ppm). The results are shown in Fig. 9 for several spots analyzed within each sorbent material. The corresponding complex spectra are grouped according to the corresponding main vibrations to exhibit the trends. The notable peak at 948–952 cm^{-1} is due to the adsorbed PO_4^{3-} [82]. Other peaks were assigned to those due to the inorganic ions HPO_4^- and CO_3^{2-} [63] while the corresponding organic vibrations can be represented by the peaks due to C(OH), bending (stretching) C-H, C-O, C=O modes at ~1010, 1080, 1130, 1281 (2950), 1450, 1740 cm^{-1} with OH stretch apparent at ~3560 cm^{-1} [83–87]. It can be seen that for the increasing concentrations, the observed presence of the corresponding dicarboxylic acids differed significantly. In particular, at 50 ppm no detectable organic vibrations were observed. Increasing the initial oxalic acid concentration to 500 ppm resulted in strong peaks due to C-O and C=O intermixed with those due to CO_3^{2-} with decreased PO_4^{3-} peak intensity, consistent with ion

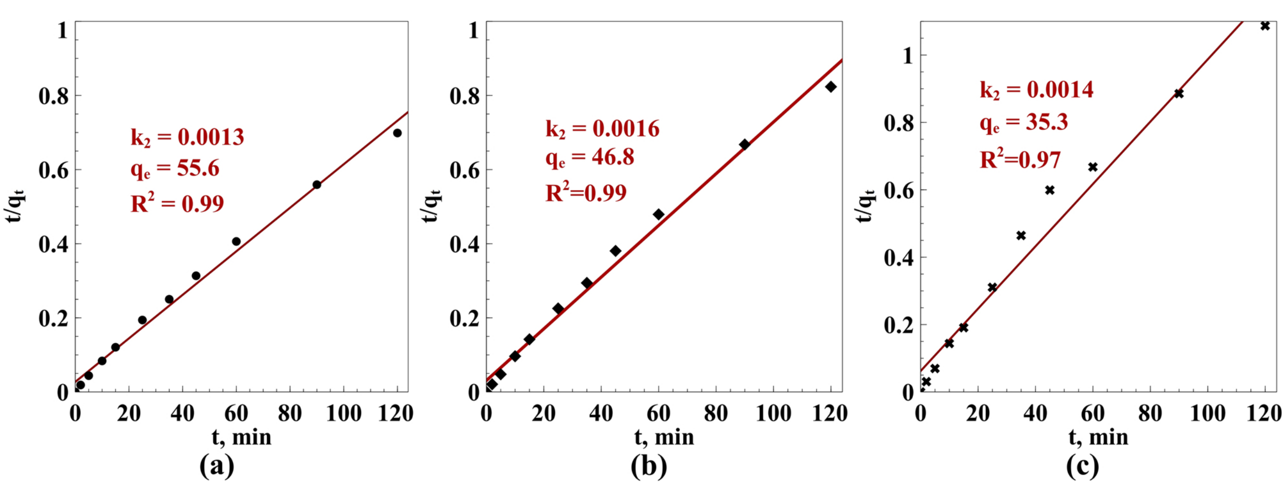

Fig. 7. The pseudo-second-order model of PO_4^{3-} adsorption on (a) LKD (1800/600 ppm LKD/MAP), (b) LKD with tartaric acid (1800/600/500 ppm LKD/MAP/TA) and (c) BA (2200/600 ppm BA/MAP).

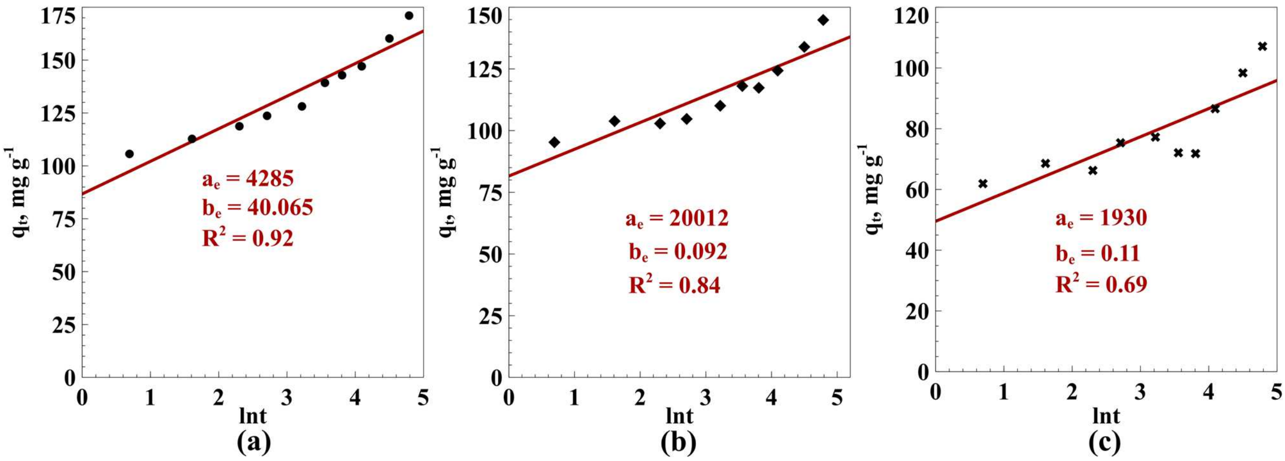

Fig. 8. The Elovich model of PO_4^{3-} adsorption on (a) LKD (1800/600 ppm LKD/MAP), (b) LKD with tartaric acid (1800/600/500 ppm LKD/MAP/TA) and (c) BA (2200/600 ppm BA/MAP).

Table 4
Comparison of phosphate removal between LKD and BA, and previously reported naturally derived adsorbent materials.

Adsorbent	q_e (mg P/g)	Source
LKD	55.6	This study
BA	35.3	This study
Goethite	32	[74]
Sepiolite	34	[20]
Akagenite	19.9	[75]
Granulated ferric hydroxide	23.3	[76]
Al-bentonite	12.7	[77]
Ca/Mg-biochar	40.4	[78]
Ca rich Carbonatation cake	20.5	[79]
Calcined sepiolite	54.4	[80]

Table 5
PO_4^{3-} removal in the presence of citric, glycolic, oxalic and citric acids on LKD and BA.

Organic acid concentration, ppm	PO_4^{3-} removal, %				
	1800/600 ppm LKD/MAP +organic acid				2200/600 ppm BA/MAP +organic acid
	Organic acid				
	tartaric	citric	glycolic	oxalic	oxalic
50	96	95	98	95	–
500	84	34	97	62	11
1000	59	34	94	42	0

chromatography measurements. Similarly, tartaric acid interacted strongly with LKD at 1000 ppm concentration in the initial solution. Glycolic acid did not inhibit PO_4^{3-} adsorption and did not exhibit strong binding with the LKD. Citric acid showed very different and unexpected behavior. While it strongly inhibited PO_4^{3-} adsorption from solution at higher concentrations of 1000 ppm, it was not measured in detectable amounts on the sample surface [88]. The lack of citric acid in the final product indicates that the PO_4^{3-} adsorption was hindered due to the surface dissolution of LKD by citric acid rather than competitive adsorption, hence, it is not present adsorbed on the solid surface. If citric acid had adsorbed on the surface and blocked the PO_4^{3-} adsorption sites, Raman spectroscopy would have detected the relevant C-H vibrations from the citrate ions, and the lack of such peaks indicates that the citric acid causes dissolution to hinder PO_4^{3-} adsorption on LKD. From pKa values for the first deprotonation of each acid oxalic acid (1.2), citric acid (3.1), and tartaric acid (2.98), show stronger acidity compared to glycolic acid (3.98) [89–92]. However, calcium tartrate is a low-solubility mineral that is known to precipitate at low Ca^{2+} concentrations, and thus, its presence in the product along with LKD is expected as it can bind to surface Ca sites [93]. Similarly, the Raman spectra shown in Fig. 9c contained peaks at 830, 911, 1480, 1630 cm^{-1} which have been reported for calcium oxalate dihydrate crystals, revealing that calcium oxalate formation can block PO_4^{3-} adsorption [94]. Therefore, a combination of organic acid adsorption on Ca-sites and adsorbent dissolution has led to the suppression of PO_4^{3-} removal by LKD.

3.5. Elemental composition and heavy metal leaching upon PO_4^{3-} adsorption and environmental safety implications

The chemical composition of the resulting effluents after the reaction of 2200/600 ppm BA/MAP and 1800/600 ppm LKD/MAP without organic acids is shown in Table 6. It can be seen that, most importantly, ~44 and 9 mg/l of P are still present in the solution, consistent with data in Fig. 1 (expressed as PO_4^{3-} and measured using ion chromatography). This is higher than that required by some USA states with heavy nutrient loading due to the agriculture, such as Wisconsin, of ~1 mg/L. This suggests the effluent needs to undergo secondary treatment to remove the residual phosphorus. This suggests that original solid material, while reconstructing physically as shown in Fig. 2c and d SEM images, largely retains its primary elemental composition.

Accumulation of heavy metals in the soil through leaching from the rapidly expanding anthropogenic sources, including but not limited to land application of fertilizers, animal manures, sewage sludge, wastewater irrigation, is of major environmental concern [95]. The corresponding concentration of heavy metals in as received BA and LKD powders was measured and is shown in Fig. 10. Six major heavy metals were detected including cadmium (Cd), lead (Pb), nickel (Ni), copper (Cu), zinc (Zn) and chromium (Cr). BA contained ~x10 higher concentrations of microelements and heavy metals with ~700 mg kg^{-1} of Zn alone, consistent with recent reports [96,97]. While some metals, such as Cu and Zn, are essential to plant growth and only toxic to plants at high concentrations, others such as Cd, Pb, Cr or Ni, have a chiefly toxic effect on living organisms. Both BA and LKD contained Cd, Pb, Cr or Ni from few to tens of ppm.

The measured concentrations of leached metals varied between LKD and BA with BA releasing more metals, especially Zn. Notably, the mobilization of the heavy metals was essentially unchanged when LKD and BA were reacted with organic acids with and without the presence of MAP (not shown), which confirms that the surface dissolution of the adsorbent occurs as discussed above, and is the main driver for releasing

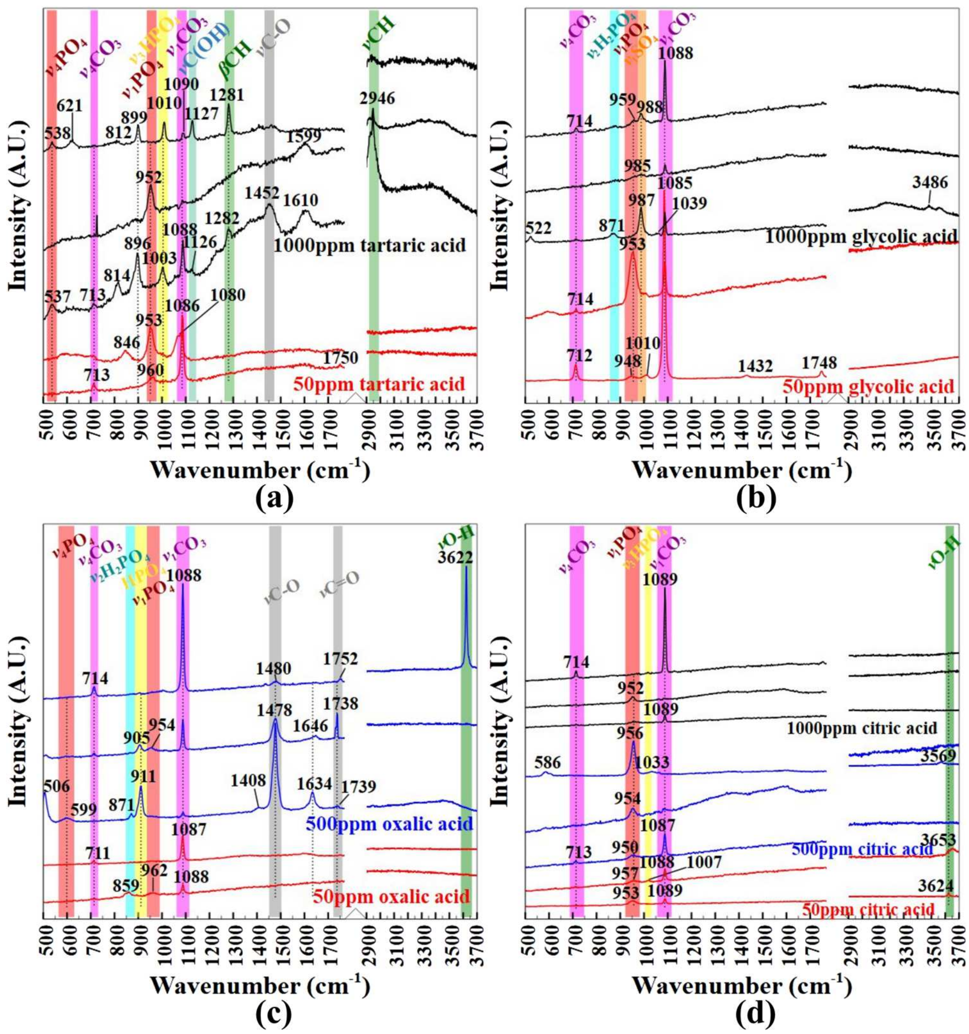

Fig. 9. 1800/600 ppm LKD/MAP reacted surfaces in the presence of (a) tartaric (b) glycolic (c) oxalic (d) citric acids at low and high initial concentrations of acids (50, 500 and 1000 ppm).

Table 6
Chemical composition of the effluents after reactions 2200/600 ppm BA/MAP and 1800/600 ppm LKD/MAP.

Element	2200/600 ppm BA/MAP effluent composition	1800/600 ppm LKD/MAP effluent composition
P, mg/l	44.5 ± 0.62	8.73 ± 0.01
K, mg/l	20.8 ± 0.74	0.935 ± 0.004
Ca, mg/l	21.3 ± 1.02	9.33 ± 0.04
Mg, mg/l	2.43 ± 0.02	0.291 ± 0.011
S, mg/l	10.3 ± 0.1	7.49 ± 0.23

heavy metals into the aqueous phase. The US EPA limits the maximum daily concentration for Zn, Cu, Cr, Ni, Pb, and Cd discharged for 0.497, 0.865, 0.746, 3.95, 1.32, and 0.474 ppm. In all cases, the concentrations of leached heavy metals were well below the regulations set forth by the US EPA as well as other regulatory agencies such as WHO and World Bank for wastewater effluents, showing that LKD can be utilized successfully for PO_4^{3-} removal in wastewater with similar organic acid conditions without interfering with legal limits of heavy metal contamination [98,99]. In the case of BA, the release of Zn was shown to be above the EPA regulated level of 0.497 ppm when citric and oxalic acids were present in 1000 ppm concentrations. However, tartaric and glycolic acids did not cause Zn release to exceed the legal limit.

4. Conclusions

Both LKD and BA are generated in large quantities and contain important major nutrients as well as regulated heavy metals. This manuscript represents work to evaluate their feasibility in PO_4^{3-} ion adsorption from aqueous solutions. Batch experiments showed that PO_4^{3-} adsorption proceeds in two regimes while kinetics were shown to fit pseudo second order mechanism. Estimated sorption capacity was 55.6 and 35.3 mg P/g for LKD and BA, respectively, comparable or higher than for other natural Ca-containing natural minerals reported in the literature. The presence of organic acids, found in wastewater, except glycolic, inhibited the amount of PO_4^{3-} ion adsorbed for the relevant acid concentration of up to 1000 ppm. Heavy metal, including Zn, Cu, Cr, Ni, Pb, and Cd, leaching was observed into the aqueous solution largely below the maximum allowable concentrations regulated by EPA. A notable exception was Zn from BA due to its high initial concentration in the material. Interestingly, the amount of the metals released varied only slightly between the experimental conditions (with or without PO_4^{3-} ion or organic acid) suggesting that the chief cause was a strong physical dissolution of the original Ca-containing material rather than competitive PO_4^{3-} ion/organic acid adsorption.

The data presented here suggest that PO_4^{3-} ion adsorption on calcium-containing waste materials takes place efficiently via chemisorption with intra-particle diffusion and external mass transfer being rate-limiting steps. This is likely related to the change in particle shape

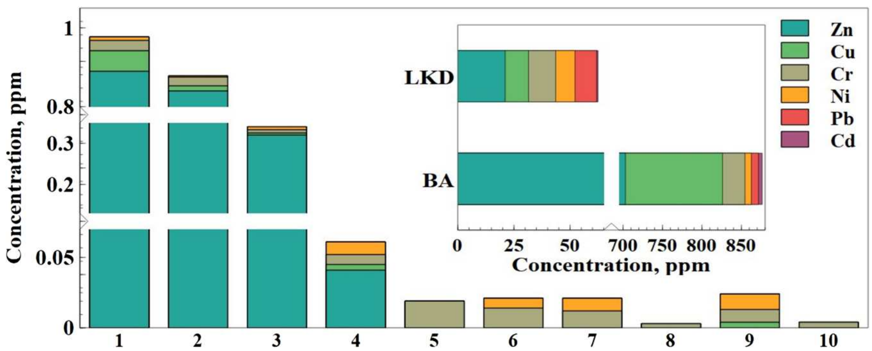

Fig. 10. Heavy metal in as received a solid BA, LKD (inset) and their concentration measured after reaction in the aqueous solution of (1) 2200/600/1000 ppm BA/MAP/oxalic acid, (2) 2200/600/1000 ppm BA/MAP/citric acid, (3) 2200/600/1000 ppm BA/MAP/tartaric acid, (4) 2200/600/1000 ppm BA/MAP/glycolic acid, (5) 2200/600 ppm BA/MAP (6) 1800/600/1000 ppm LKD/MAP/oxalic acid, (7) 1800/600/1000 ppm LKD/MAP/citric acid, (8) 1800/600/1000 ppm LKD/MAP/tartaric acid, (9) 1800/600/1000 ppm LKD/MAP/glycolic acid, (10) 1800/600 ppm LKD/MAP. The maximum standard deviation measured was 8.4%.

which needs to take place via sufficient dissolution for efficient PO_4^{3-} ion absorption. This has practical implications if the industrial scale adsorption process efficiency where potentially longer batch reaction times can be avoided if these sorptive materials are first hydrated in a slurry to achieve the necessary absorption capacity. Finally, the disposal of the batch solution from the sorption process can be performed via discharge since no major heavy metal concentration increase is observed during the leaching process.

CRediT authorship contribution statement

Donata Drapanauskaite: Conceptualization, Investigation, Visualization, Writing – original draft, Writing – review & editing, Resources, **Kristina Buneviciene:** Conceptualization, Investigation, Visualization, Resourcesa, **Manoj Silva:** Investigation, Writing – original draft, Writing – review & editing, **Alvyra Slepetiene:** Investigation, **Jonas Baltrusaitis:** Conceptualization, Writing – original draft, Writing – review & editing, Resources, Supervision, Funding acquisition.

Declaration of Competing Interest

The authors declare that they have no known competing financial interests or personal relationships that could have appeared to influence the work reported in this paper.

Acknowledgments

This material is based on work supported by the National Science Foundation under grant no. CHE 1710120. We gratefully acknowledge Prof. John Fox and PhD student Pan Ni for SEM/EDS use and Dr. Lohit Sharma for BET experiments.

References

[1] J. Fiksel, A framework for sustainable materials management, JOM 58 (2006) 15–22, https://doi.org/10.1007/s11837-006-0047-3.
[2] J. Baltrusaitis, A.M. Sviklas, Phase composition of aqueous urea–ammonium nitrate (UAN)–zinc nitrate solutions for sustainable reuse of zinc containing industrial pigment waste, ACS Sustain. Chem. Eng. 3 (2015) 950–958, https://doi.org/10.1021/acssuschemeng.5b00067.
[3] H. Zhang, M. Frey, C. Navizaga, C. Lenzo, J. Taborda, W. Taifan, A. Sadeghnejad, A.M.A.M. Sviklas, J. Baltrusaitis, Dairy wastewater for production of chelated biodegradable Zn micronutrient fertilizers, ACS Sustain. Chem. Eng. 4 (2016) 1722–1727, https://doi.org/10.1021/acssuschemeng.5b01688.
[4] J. Baltrusaitis, A.M.M. Sviklas, Urea–ammonium nitrate aqueous solutions containing cu micronutrient obtained from cable manufacturing solid waste, ACS Sustain. Chem. Eng. 3 (2015) 1544–1550, https://doi.org/10.1021/acssuschemeng.5b00241.
[5] M.M. Rahman, M.A.M. Salleh, U. Rashid, A. Ahsan, M.M. Hossain, C.S. Ra, Production of slow release crystal fertilizer from wastewaters through struvite crystallization – A review, Arab. J. Chem. 7 (2014) 139–155, https://doi.org/10.1016/j.arabjc.2013.10.007.
[6] J. Shu, R. Liu, Z. Liu, H. Chen, J. Du, C. Tao, Solidification/stabilization of electrolytic manganese residue using phosphate resource and low-grade MgO/CaO, J. Hazard. Mater. 317 (2016) 267–274, https://doi.org/10.1016/j.jhazmat.2016.05.076.
[7] A. Capdevielle, E. Sýkorová, B. Biscans, F. Béline, M.-L. Daumer, Optimization of struvite precipitation in synthetic biologically treated swine wastewater–determination of the optimal process parameters, J. Hazard. Mater. 244–245 (2013) 357–369, https://doi.org/10.1016/j.jhazmat.2012.11.054.
[8] L.-W. Deng, P. Zheng, Z.-A. Chen, Anaerobic digestion and post-treatment of swine wastewater using IC–SBR process with bypass of raw wastewater, Process Biochem. 41 (2006) 965–969, https://doi.org/10.1016/j.procbio.2005.10.022.
[9] L.E. de-Bashan, Y. Bashan, Recent advances in removing phosphorus from wastewater and its future use as fertilizer (1997-2003), Water Res. 38 (2004) 4222–4246, https://doi.org/10.1016/j.watres.2004.07.014.
[10] A. Korchef, H. Saidou, M. Ben Amor, Phosphate recovery through struvite precipitation by CO_2 removal: effect of magnesium, phosphate and ammonium concentrations, J. Hazard. Mater. 186 (2011) 602–613, https://doi.org/10.1016/j.jhazmat.2010.11.045.
[11] D. Cordell, S. White, Peak phosphorus: clarifying the key issues of a vigorous debate about long-term phosphorus security, Sustainability 3 (2011) 2027–2049, https://doi.org/10.3390/su3102027.
[12] A.T.K. Tran, Y. Zhang, D. De Corte, J.-B. Hannes, W. Ye, P. Mondal, N. Jullok, B. Meesschaert, L. Pinoy, B. Van der Bruggen, P-recovery as calcium phosphate from wastewater using an integrated selectrodialysis/crystallization process, J. Clean. Prod. 77 (2014) 140–151, https://doi.org/10.1016/j.jclepro.2014.01.069.
[13] M. Silva, V. Murzin, L. Zhang, J.P. Baltrus, J. Baltrusaitis, Transition metal doped MgO nanoparticles for nutrient recycling: An alternate Mg source for struvite synthesis from wastewater, Environ. Sci. Nano. 7 (2020) 3482–3496, https://doi.org/10.1039/d0en00660b.
[14] S. Takagi, M. Mathew, W.E. Brown, Structure of ammonium calcium phosphate heptahydrate, Ca(NH4)PO4.7H2O, Acta Crystallogr. Sect. C Cryst. Struct. Commun. 40 (1984) 1111–1113, https://doi.org/10.1107/S0108270184006995.
[15] A. Rabinovich, A.A. Rouff, B. Lew, M.V. Ramlogan, Aerated fluidized bed treatment for phosphate recovery from dairy and swine wastewater, ACS Sustain. Chem. Eng. 6 (2018) 652–659, https://doi.org/10.1021/acssuschemeng.7b02990.
[16] R.R. Pahunang, F.C. Ballesteros, M.D.G. de Luna, A.C. Vilando, M.-C. Lu, Optimum recovery of phosphate from simulated wastewater by unseeded fluidized-bed crystallization process, Sep. Purif. Technol. 212 (2019) 783–790, https://doi.org/10.1016/j.seppur.2018.11.087.
[17] H. Dai, X. Lu, Y. Peng, Z. Yang, H. Zhsssu, Effects of supersaturation control strategies on hydroxyapatite (HAP) crystallization for phosphorus recovery from wastewater, Environ. Sci. Pollut. Res. 24 (2017) 5791–5799, https://doi.org/10.1007/s11356-016-8236-2.
[18] G. Wernet, C. Bauer, B. Steubing, J. Reinhard, E. Moreno-Ruiz, B. Weidema, The ecoinvent database version 3 (part I): overview and methodology, Int. J. Life Cycle Assess. 21 (2016) 1218–1230, https://doi.org/10.1007/s11367-016-1087-8.
[19] Ostara, Ostara and EPCOR Partner to Build Nutrient Recovery Technology Facility, ⟨Http://Ostara.Com/Project/Ostara-and-Epcor-Partner-to-Build-Nutrient-Recovery-Technology-Facility/⟩. (2014).
[20] H. Yin, Y. Yun, Y. Zhang, C. Fan, Phosphate removal from wastewaters by a naturally occurring, calcium-rich sepiolite, J. Hazard. Mater. 198 (2011) 362–369, https://doi.org/10.1016/j.jhazmat.2011.10.072.
[21] I. Perassi, L. Borgnino, Adsorption and surface precipitation of phosphate onto CaCO3–montmorillonite: effect of pH, ionic strength and competition with humic acid, Geoderma 232–234 (2014) 600–608, https://doi.org/10.1016/j.geoderma.2014.06.017.
[22] H. Yin, J. Zhu, In situ remediation of metal contaminated lake sediment using naturally occurring, calcium-rich clay mineral-based low-cost amendment, Chem. Eng. J. 285 (2016) 112–120, https://doi.org/10.1016/j.cej.2015.09.108.
[23] G.S. dos Reis, B. Grigore Cazacliu, C. Rodriguez Correa, E. Ovsyannikova, A. Kruse, C. Hoffmann Sampaio, E.C. Lima, G.L. Dotto, Adsorption and recovery of phosphate from aqueous solution by the construction and demolition wastes sludge and its potential use as phosphate-based fertiliser, J. Environ. Chem. Eng. 8 (2020), 103605, https://doi.org/10.1016/j.jece.2019.103605.
[24] M. Liu, C. Wang, J. Guo, L. Zhang, Removal of phosphate from wastewater by lanthanum modified bio-ceramisite, J. Environ. Chem. Eng. 9 (2021), 106123, https://doi.org/10.1016/j.jece.2021.106123.
[25] J.-K. Kang, E.-J. Seo, C.-G. Lee, S.-J. Park, Fe-loaded biochar obtained from food waste for enhanced phosphate adsorption and its adsorption mechanism study via

spectroscopic and experimental approach, J. Environ. Chem. Eng. 9 (2021), 105751, https://doi.org/10.1016/j.jece.2021.105751.
[26] P. Myllymäki, J. Pesonen, E.-T. Nurmesniemi, H. Romar, P. Tynjälä, T. Hu, U. Lassi, The use of industrial waste materials for the simultaneous removal of ammonium nitrogen and phosphate from the anaerobic digestion reject water, Waste Biomass Valoriz. 11 (2020) 4013–4024, https://doi.org/10.1007/s12649-019-00724-8.
[27] F. Lamers, M. Cremers, D. Matschegg, C. Schmidl, K. Hannam, P. Hazlett, S. Madrali, B.P. Dam, R. Roberto, R. Mager, K. Davidsson, N. Bech, H.-J. Feuerborn, A. Saraber, Options for increased use of ash from biomass combustion and co-firing, IEA Bioenergy (2018) 1–61.
[28] K. Chojnacka, K. Moustakas, A. Witek-Krowiak, Bio-based fertilizers: a practical approach towards circular economy, Bioresour. Technol. 122223 (2019), https://doi.org/10.1016/j.biortech.2019.122223.
[29] S.V. Vassilev, D. Baxter, L.K. Andersen, C.G. Vassileva, An overview of the composition and application of biomass ash. Part 1. Phase-mineral and chemical composition and classification, Fuel 105 (2013) 40–76, https://doi.org/10.1016/j.fuel.2012.09.041.
[30] S.V. Vassilev, D. Baxter, L.K. Andersen, C.G. Vassileva, An overview of the composition and application of biomass ash.: Part 2. Potential utilisation, technological and ecological advantages and challenges, Fuel 105 (2013) 19–39, https://doi.org/10.1016/j.fuel.2012.10.001.
[31] G.I. Ågren, Stoichiometry and nutrition of plant growth in natural communities, Annu. Rev. Ecol. Evol. Syst. 39 (2008) 153–170, https://doi.org/10.1146/annurev.ecolsys.39.110707.173515.
[32] F.J. Maathuis, Physiological functions of mineral macronutrients, Curr. Opin. Plant Biol. 12 (2009) 250–258, https://doi.org/10.1016/j.pbi.2009.04.003.
[33] C.O. Dimkpa, P.S. Bindraban, Fortification of micronutrients for efficient agronomic production: a review, Agron. Sustain. Dev. 36 (2016), 7, https://doi.org/10.1007/s13593-015-0346-6.
[34] T. Karak, R.M. Bhagat, P. Bhattacharyya, Municipal solid waste generation, composition, and management: the world scenario, Crit. Rev. Environ. Sci. Technol. 42 (2012) 1509–1630, https://doi.org/10.1080/10643389.2011.569871.
[35] R. Barbosa, N. Lapa, H. Lopes, A. Morujo, B. Mendes, Removal of phosphorus from wastewaters by biomass ashes, Water Sci. Technol. (2013) 2019–2028, https://doi.org/10.2166/wst.2013.455.
[36] A. Alzeyadi, N. Al-ansari, J. Laue, A. Alattabi, Study of biomass bottom ash efficiency as phosphate sorbent material, Civ. Eng. J. 5 (2019) 2392–2401.
[37] K. Kuma, S. Nakabayashi, Y. Suzuki, I. Kudo, K. Matsunaga, Photo-reduction of Fe (III) by dissolved organic substances and existence of Fe(II) in seawater during spring blooms, Mar. Chem. 37 (1992) 15–27, https://doi.org/10.1016/0304-4203(92)90054-E.
[38] N. Eleutheria, I. Maria, T. Vasiliki, E. Alexandros, A. Alexandros, D. Vasileios, Energy recovery and treatment of winery wastes by a compact anaerobic digester, Waste Biomass Valoriz. 7 (2016) 799–805, https://doi.org/10.1007/s12649-016-9541-1.
[39] J.A. Pérez-Serradilla, M.D.L. de Castro, Role of lees in wine production: a review, Food Chem. 111 (2008) 447–456, https://doi.org/10.1016/j.foodchem.2008.04.019.
[40] J. Yang, L. Zhong, L. Liu, Coupling of tartaric acid-promoted soil dissolution and Cr (VI) reduction in an Oxisol, J. Geochem. Explor 125 (2013) 138–143, https://doi.org/10.1016/j.gexplo.2012.12.003.
[41] T. Cai, S.Y. Park, Y. Li, Nutrient recovery from wastewater streams by microalgae: status and prospects, Renew. Sustain. Energy Rev. 19 (2013) 360–369, https://doi.org/10.1016/j.rser.2012.11.030.
[42] P. Ni, J.T. Fox, Synthesis and appraisal of a hydroxyapatite/pectin hybrid material for zinc removal from water, RSC Adv. 9 (2019) 21095–21105, https://doi.org/10.1039/c9ra03710a.
[43] W.H. Chesner, R.J. Collins, M.H. MacKay, J. Emery, User Guidelines for Waste and By-Product Materials in Pavement Construction, 1998.
[44] R.J. Collins, J. Emery, Kiln Dust-Fly Ash Systems for Highway Bases and Subbases, 1983, 1–142.
[45] M.M. El-Attar, D.M. Sadek, A.M. Salah, Recycling of high volumes of cement kiln dust in bricks industry, J. Clean. Prod. 143 (2017) 506–515, https://doi.org/10.1016/J.JCLEPRO.2016.12.082.
[46] M.A.M. Ali, H.S. Yang, Utilization of cement kiln dust in industry cement bricks, Geosyst. Eng. 14 (2011) 29–34, https://doi.org/10.1080/12269328.2011.10541327.
[47] N. Muhammad, G. Zvobgo, G. ping Zhang, A review: the beneficial effects and possible mechanisms of aluminum on plant growth in acidic soil, J. Integr. Agric. 18 (2019) 1518–1528, https://doi.org/10.1016/S2095-3119(18)61991-4.
[48] C.D. Foy, R.L. Chaney, M.C. White, The physiology of metal toxicity in plants, Annu. Rev. Plant Physiol. 29 (1978) 511–566, https://doi.org/10.1146/annurev.pp.29.060178.002455.
[49] J. Morrissey, M.Lou Guerinot, Iron uptake and transport in plants: the good, the bad, and the ionome, Chem. Rev. 109 (2009) 4553–4567, https://doi.org/10.1021/cr900112r.
[50] M. Nikolic, R. Kastori, Effect of bicarbonate and Fe supply on Fe nutrition of grapevine, J. Plant Nutr. 23 (2000) 1619–1627, https://doi.org/10.1080/01904160009382128.
[51] N.M. Sigvardsen, L.M. Ottosen, Characterization of coal bio ash from wood pellets and low-alkali coal fly ash and use as partial cement replacement in mortar, Cem. Concr. Compos. 95 (2019) 25–32, https://doi.org/10.1016/j.cemconcomp.2018.10.005.
[52] S. Liodakis, G. Katsigiannis, G. Kakali, Ash properties of some dominant Greek forest species, Thermochim. Acta 437 (2005) 158–167, https://doi.org/10.1016/j.tca.2005.06.041.
[53] I. Carevic, M. Serdar, N. Štirmer, N. Ukrainczyk, Preliminary screening of wood biomass ashes for partial resources replacements in cementitious materials, J. Clean. Prod. 229 (2019) 1045–1064, https://doi.org/10.1016/j.jclepro.2019.04.321.
[54] D. Bajare, G. Bumanis, G. Shakhmenko, J. Justs, Obtaining composition of geopolymers (alkali activated binders) from local industrial wastes, Civ. Eng. '11 - 3rd Int. Sci. Conf. Proc. 3, 2011, 50–56.
[55] S.A. Markgraf, R.J. Reeder, High-temperature structure refinements of calcite and magnesite, Am. Mineral. 70 (1985) 590–600.
[56] L. Levien, C.T. Prewitt, D.J. Weidner, C.T. Prewir, D.J. Weidner, Structure and elastic properties of quartz at pressure, Am. Mineral. 65 (1980) 920–930.
[57] L. Desgranges, D. Grebille, G. Calvarin, G. Chevrier, N. Floquet, J. -C. Niepce, Hydrogen thermal motion in calcium hydroxide: Ca(OH)2, Acta Crystallogr. Sect. B 49 (1993) 812–817, https://doi.org/10.1107/S0108768193003556.
[58] B. Lu, D. Kiani, W. Taifan, D. Barauskas, K. Honer, L. Zhang, J. Baltrusaitis, Spatially resolved product speciation during struvite synthesis from magnesite (MgCO 3) particles in ammonium (NH 4 +) and phosphate (PO 4 3–) aqueous solutions, J. Phys. Chem. C 123 (2019) 8908–8922, https://doi.org/10.1021/acs.jpcc.8b12252.
[59] D. Kiani, Y. Sheng, B. Lu, D. Barauskas, K. Honer, Z. Jiang, J. Baltrusaitis, Transient struvite formation during stoichiometric (1:1) NH4+ and PO43– adsorption/reaction on magnesium oxide (MgO) particles, ACS Sustain. Chem. Eng. 7 (2018) 1545–1556, https://doi.org/10.1021/acssuschemeng.8b05318.
[60] A.C. Chapman, D.A. Long, D.T.L. Jones, Spectra of phosphorous compounds—II, Spectrochim. Acta 21 (1965) 633–640, https://doi.org/10.1016/0371-1951(65)80019-4.
[61] A.C. Chapman, L.E. Thirlwell, Spectra of phosphorus compounds—I the infra-red spectra of orthophosphates, Spectrochim. Acta 20 (1964) 937–947, https://doi.org/10.1016/0371-1951(64)80094-1.
[62] J.A. Stammeier, B. Purgstaller, D. Hippler, V. Mavromatis, M. Dietzel, In-situ Raman spectroscopy of amorphous calcium phosphate to crystalline hydroxyapatite transformation, MethodsX 5 (2018) 1241–1250, https://doi.org/10.1016/J.MEX.2018.09.015.
[63] D. Kiani, M. Silva, Y. Sheng, J. Baltrusaitis, Experimental insights into the genesis and growth of struvite particles on low-solubility dolomite mineral surfaces, J. Phys. Chem. C 123 (2019) 25135–25145, https://doi.org/10.1021/acs.jpcc.9b05292.
[64] V.V. Nosenko, A.M. Yaremko, V.M. Dzhagan, I.P. Vorona, Y.A. Romanyuk, I. V. Zatovsky, Nature of some features in Raman spectra of hydroxyapatite-containing materials, J. Raman Spectrosc. 47 (2016) 726–730, https://doi.org/10.1002/jrs.4883.
[65] K.A. Syed, S.F. Pang, Y. Zhang, G. Zeng, Y.H. Zhang, Micro-Raman observation on the HPO42- association structures in an individual dipotassium hydrogen phosphate (K2HPO 4) droplet, J. Phys. Chem. A 116 (2012) 1558–1564, https://doi.org/10.1021/jp2110743.
[66] T. Mouri, M. Enami, Raman spectroscopic study of olivine-group minerals, J. Mineral. Petrol. Sci. 103 (2008) 100–104, https://doi.org/10.2465/jmps.071015.
[67] S. Tang, Z. Wang, D. Yuan, C. Zhang, Y. Rao, Z. Wang, K. Yin, Ferrous ion-tartaric acid chelation promoted calcium peroxide fenton-like reactions for simulated organic wastewater treatment, J. Clean. Prod. 268 (2020), 122253, https://doi.org/10.1016/j.jclepro.2020.122253.
[68] T. Colin, A. Bories, Y. Sire, R. Perrin, Treatment and valorisation of winery wastewater by a new biophysical process (ECCF®), Water Sci. Technol. 51 (2005) 99–106, https://doi.org/10.2166/wst.2005.0012.
[69] J.F. De Rooij, J.C. Heughebaert, G.H. Nancollas, A ph study of calcium phosphate seeded precipitation, J. Colloid Interface Sci. 100 (1984) 350–358, https://doi.org/10.1016/0021-9797(84)90440-5.
[70] S. Azizian, Kinetic models of sorption: a theoretical analysis, J. Colloid Interface Sci. 276 (2004) 47–52, https://doi.org/10.1016/j.jcis.2004.03.048.
[71] I.S. McLintock, The elovich equation in chemisorption kinetics, Nature 216 (1967) 1204–1205, https://doi.org/10.1038/2161204a0.
[72] Y.S. Ho, G. Mckay, Pseudo-second order model for sorption processes, 1999.
[73] M. Silva, J. Baltrusaitis, A review of phosphate adsorption on Mg-containing materials: kinetics, equilibrium, and mechanistic insights, Environ. Sci. Water Res. Technol. (2020), https://doi.org/10.1039/D0EW00679C.
[74] H. Siwek, A. Bartkowiak, M. Włodarczyk, Adsorption of phosphates from aqueous solutions on alginate/goethite hydrogel composite, Water 11 (2019), 633, https://doi.org/10.3390/w11040633.
[75] C.-K. Na, G.-Y. Park, H.J. Park, Applicability of ferric(III) hydroxide as a phosphate-selective adsorbent for sewage treatment, Water Sci. Technol. 83 (2021) 2911–2920, https://doi.org/10.2166/WST.2021.180.
[76] A. Genz, A. Kornmüller, M. Jekel, Advanced phosphorus removal from membrane filtrates by adsorption on activated aluminium oxide and granulated ferric hydroxide, Water Res. 38 (2004) 3523–3530, https://doi.org/10.1016/J.WATRES.2004.06.006.
[77] L.G. Yan, Y.Y. Xu, H.Q. Yu, X.D. Xin, Q. Wei, B. Du, Adsorption of phosphate from aqueous solution by hydroxy-aluminum, hydroxy-iron and hydroxy-iron–aluminum pillared bentonites, J. Hazard. Mater. 179 (2010) 244–250, https://doi.org/10.1016/J.JHAZMAT.2010.02.086.
[78] W. Deng, D. Zhang, X. Zheng, X. Ye, X. Niu, Z. Lin, M. Fu, S. Zhou, Adsorption recovery of phosphate from waste streams by Ca/Mg-biochar synthesis from marble waste, calcium-rich sepiolite and bagasse, J. Clean. Prod. 288 (2021), 125638, https://doi.org/10.1016/J.JCLEPRO.2020.125638.
[79] H. Arslanoglu, Production of low-cost adsorbent with small particle size from calcium carbonate rich residue carbonatation cake and their high performance

phosphate adsorption applications, J. Mater. Res. Technol. 11 (2021) 428–447, https://doi.org/10.1016/J.JMRT.2021.01.054.
[80] S.H. Hong, A.M. Ndingwan, S.C. Yoo, C.G. Lee, S.J. Park, Use of calcined sepiolite in removing phosphate from water and returning phosphate to soil as phosphorus fertilizer, J. Environ. Manag. 270 (2020), 110817, https://doi.org/10.1016/J.JENVMAN.2020.110817.
[81] H. Colas, L. Bonhomme-Coury, C.C. Diogo, F. Tielens, F. Babonneau, C. Gervais, D. Bazin, D. Laurencin, M.E. Smith, J.V. Hanna, M. Daudon, C. Bonhomme, Whewellite, CaC2O4 center dot H2O: structural study by a combined NMR, crystallography and modelling approach, Crystengcomm 15 (2013) 8840–8847, https://doi.org/10.1039/c3ce41201f.
[82] E. Kirinovic, A.R. Leichtfuss, C. Navizaga, H. Zhang, J.D.S. Christus, J. Baltrusaitis, Spectroscopic and microscopic identification of the reaction products and intermediates during the struvite (MgNH4PO4·6H2O) formation from magnesium oxide (MgO) and magnesium carbonate (MgCO3) microparticles, ACS Sustain. Chem. Eng. 5 (2017) 1567–1577, https://doi.org/10.1021/acssuschemeng.6b02327.
[83] Y. Ebisuzaki, S.M. Angel, Raman study of hydrogen bonding in α and β-oxalic acid dihydrate, J. Raman Spectrosc. 11 (1981) 306–311, https://doi.org/10.1002/jrs.1250110416.
[84] R. Bhattacharjee, Y.S. Jain, H.D. Bist, Laser Raman and infrared spectra of tartaric acid crystals, J. Raman Spectrosc. 20 (1989) 91–97, https://doi.org/10.1002/jrs.1250200206.
[85] J.H. Hibben, The raman spectra of oxalic acid, J. Chem. Phys. 3 (1935) 675–679, https://doi.org/10.1063/1.1749575.
[86] T.A. Shippey, Vibrational studies in aqueous solutions: part II. The acid oxalate ion and oxalic acid, J. Mol. Struct. 65 (1980) 71–86, https://doi.org/10.1016/0022-2860(80)85181-7.
[87] Z. Huang, X. Chen, Y. Li, J. Chen, J. Lin, J. Wang, J. Lei, R. Chen, Quantitative determination of citric acid in seminal plasma by using raman spectroscopy, Appl. Spectrosc. 67 (2013) 757–760, https://doi.org/10.1366/12-06902.
[88] M. Lindegren, P. Persson, Competitive adsorption between phosphate and carboxylic acids: quantitative effects and molecular mechanisms, Eur. J. Soil Sci. 60 (2009) 982–993, https://doi.org/10.1111/j.1365-2389.2009.01171.x.
[89] R.I. Gelb, Conductometric determination of pKa values—oxalic and squaric acids, Anal. Chem. 43 (1971) 1110–1113, https://doi.org/10.1021/ac60303a028.
[90] U. Domańska, A. Pobudkowska, A. Pelczarska, P. Gierycz, pKa and solubility of drugs in water, ethanol, and 1-octanol, J. Phys. Chem B (2009) 8941–8947, https://doi.org/10.1021/jp900468w.
[91] L.F. Nims, The ionization constant of glycolic acid from 0 to 50°, J. Am. Chem. Soc. 58 (1936) 987–989, https://doi.org/10.1021/ja01297a043.
[92] D.C. Carpenter, G.L. Mack, The solubility of potassium acid tartrate. I. In tartaric acid and dipotassium tartrate solutions, J. Am. Chem. Soc. 56 (1934) 311–313, https://doi.org/10.1021/ja01317a013.
[93] R.S. Jackson, Postfermentation Treatments and Related Topics, in: Wine Sci, Elsevier, 2008, pp. 418–519, https://doi.org/10.1016/b978-012373646-8.50011-1.
[94] C. Frausto-Reyes, S. Loza-Cornejo, T. Terrazas, M. De La Luz Miranda-Beltrán, X. Aparicio-Fernández, B.M. López-Mací, S.E. Morales-Martínez, M. Ortiz-Morales, Raman spectroscopy study of calcium oxalate extracted from cacti stems, Appl. Spectrosc. 68 (2014) 1260–1265, https://doi.org/10.1366/14-07485.
[95] R.A. Wuana, F.E. Okieimen, Heavy metals in contaminated soils: a review of sources, chemistry, risks and best available strategies for remediation, ISRN Ecol. 2011 (2011) 1–20, https://doi.org/10.5402/2011/402647.
[96] K. Buneviciene, D. Drapanauskaite, R. Mazeika, V. Tilvikiene, J. Baltrusaitis, Granulated biofuel ash as a sustainable source of plant nutrients, Waste Manag. Res. J. Sustain. Circ. Econ. (2020), 0734242×2094895, https://doi.org/10.1177/0734242×20948952.
[97] D. Drapanauskaite, K. Buneviciene, R. Repsiene, R. Mazeika, J. Navea, J. Baltrusaitis, Physicochemical characterization of pelletized lime kiln dust as potential liming material for acidic soils, Waste Biomass Valoriz. (2020) https://doi.org/10.1007/s12649-020-01107-0. https://doi.org/10.1007/s12649-020-01107-0.
[98] G.K. Kinuthia, V. Ngure, D. Beti, R. Lugalia, A. Wangila, L. Kamau, Levels of heavy metals in wastewater and soil samples from open drainage channels in Nairobi, Kenya: community health implication, Sci. Rep. 10 (2020) 1–13, https://doi.org/10.1038/s41598-020-65359-5.
[99] Electronic Code of Federal Regulations (eCFR) Title 40, n.d.